Growth and characterization of well aligned densely packed IrO$_2$ nanocrystals on sapphire via reactive sputtering

Growth and characterization of well aligned densely packed IrO$_2$ nanocrystals on sapphire via reactive sputtering

Alexandru Korotcov[1], Ying-Sheng Huang[1,4], Dah-Shyang Tsai[2] and Kwong-Kau Tiong[3]

[1] Department of Electronic Engineering, National Taiwan University of Science and Technology, 43 Keelung Road, Section 4, Taipei, 106, Taiwan
[2] Department of Chemical Engineering, National Taiwan University of Science and Technology, 43 Keelung Road, Section 4, Taipei, 106, Taiwan
[3] Department of Electrical Engineering, National Taiwan Ocean University, 2 Pei-Ning Road, Keelung, 202, Taiwan

E-mail: ysh@et.ntust.edu.tw

Abstract

Well aligned densely packed IrO$_2$ nanocrystals (NCs) have been grown on sapphire (SA) substrates with different orientations by reactive magnetron sputtering using an Ir metal target. The surface morphology, structural and spectroscopic properties of the as-deposited NCs were characterized using field-emission scanning electron microscopy (FESEM), x-ray diffraction (XRD), x-ray photoelectron spectroscopy (XPS) and micro-Raman spectroscopy. FESEM micrographs reveal that NCs with parallel in-plane alignment were gown on SA(001), vertically aligned NCs were grown on SA(100), while the NCs on SA(012) and SA(110) contained, respectively, single- and double-aligned directions with a tilt angle of ∼35° from the normal to the substrates. The XRD results indicate that the NCs are (100), (001), and (101) oriented on SA(001), SA(001), and SA(012)/SA(110) substrates, respectively. A strong substrate effect on the alignment of the IrO$_2$ NCs growth has been demonstrated and the probable mechanism for the formation of these NCs has been discussed. XPS analyses show the coexistence of higher oxidation states of iridium in the as-grown IrO$_2$ NCs. The Raman spectra show the red-shift and asymmetric peak broadening with a low frequency tail of the IrO$_2$ signatures with respect to that of the bulk counterpart, which are attributed to both the size and residual stress effects.

(Some figures in this article are in colour only in the electronic version)

[4] Author to whom any correspondence should be addressed.

1. Introduction

Recently, nanoscaled materials such as wires, rods, belts, and tubes have become the focus of intensive research owing to their fundamental interest in science and potential in fabrication nanodevices [1–3]. The development of nanodevices might benefit from the unique morphology, huge surface area and high aspect ratio of nanocrystals (NCs). A wide range of the nanosized oxide materials is currently the focus of a rapidly growing scientific community. The electrically insulating and/or semiconducting oxides of nanostructured SiO_2 [4], TiO_2 [5], SnO_2 [6], GeO_2 [7], Ga_2O_3 [8], and VO_x [9] have been synthesized and studied. Among the numerous metallic oxides, the electrically conducting iridium dioxide (IrO_2) belongs to a group of materials with unique properties [10], whose nanophases are not well cultivated and required extensive investigation.

IrO_2 belongs to the family of conductive oxides crystallized in the tetragonal rutile structure [11]. Single-crystalline IrO_2 shows metallic behaviour in electrical and optical properties [12–14]. Owing to the conductive nature, high thermal and chemical stability, and effective diffusion barrier for oxygen, IrO_2 has been an attractive material for sensing material in pH sensors [15–17], for acidity and basicity determination in a non-aqueous industrial lubricant environment [18], durable electrodes for chlorine and oxygen evolution [19–21], excellent diffusion barrier and suitable electrode material in ferroelectrics for nonvolatile memory devices [12, 22, 23], optical switching layers in electrochromic displays [24, 25], and an emitter material in field emission cathodes for vacuum microelectronic devices and field emission displays [26–29].

As a result of these diverse applications, there is a growing need to develop easy and reliable methods for growing different IrO_2 phases as micro- or nanophase forms. Various methods such as reactive magnetron sputtering [13, 14, 30], pulsed laser deposition [31, 32], solution growth [20, 33], thermal preparation [34, 35], and metal–organic chemical vapour deposition (MOCVD) [36, 37] have been employed for this purpose. Recently, MOCVD has been successfully employed for the growth of IrO_2 one-dimensional nanostructures on different substrates by the authors of references [38–40]. However, MOCVD generally requires multiple processing steps to fabricate nanostructures. It is difficult to have proper control of these processes; for example, the properties of the precursor might change after a few runs of the growth. On the other hand, reactive rf magnetron sputtering is a simple method to fabricate large area structures, which has several advantages, including better control of the growth conditions and a single deposition step to obtain the nanostructures.

In this work, we report the deposition of well aligned densely packed IrO_2 NCs by reactive sputtering using an Ir metal target. The growth behaviour of IrO_2 is found to be highly correlated with the pressure, rf power, substrate temperature, and orientations of the substrates. The surface morphology and structural and spectroscopic properties of the as-deposited NCs were examined by using field-emission scanning electron microscopy (FESEM), x-ray diffraction (XRD), and micro-Raman investigation. A strong substrate effect on the alignment of the IrO_2 NCs is observed, and the probable mechanism for the formation of NCs structure will be discussed. The relative intensities of the observed Raman modes were studied by analysing the Raman-active modes in the tetragonal rutile structure for the different planes of NCs [(100), (001), (101)]. The red-shift and asymmetric broadening of Raman line shape have been analysed by the modified spatial correlation (MSC) model and attributed to both the size and residual stress effects.

2. Experimental details

2.1. Growth of iridium dioxide nanocrystals

Iridium dioxide NC deposition was carried out using a home-made high vacuum rf magnetron sputtering system. A schematic diagram of the system is shown in figure 1. The sputtering
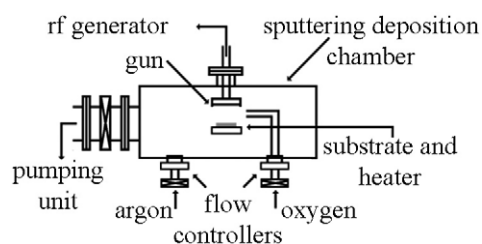
Figure 1. Schematic diagram of the rf magnetron sputtering system.

gun has a standard circular planar magnetron. The sputtering target was a 1 inch Ir (99.95%) metal. The substrates used in this study were different orientations of sapphire (SA): SA(001), SA(100), SA(012), and SA(110). All wafers had the dimensions $\sim 10 \times 10$ mm^2 and at least one side of each wafer was polished. Each substrate was pretreated through a standard cleansing procedure: consecutive cleansing with acetone and methanol in an ultrasonic bath for 10 min to prevent any contamination on the substrate surface. A manually controlled shutter was located in front of the target. The sputtering power supply had a maximum output of 300 W. Two separate gas lines, each equipped with a mass flow controller, were used to control the Ar and O$_2$ flow rates with an accuracy of 0.1 standard cubic centimetres per minute (sccm) for both gases. The sample holder was approximately 45 mm from the target and can be heated to a maximum temperature of 550 °C. To promote uniform transfer of heat to the substrates, a thin coating of melted In was placed between the substrate and the sample holder. Care was being taken to confine all the In metal only to the back of the substrate.

The sputtering chamber was evacuated with a turbo-molecular pump and had a base pressure of $\sim 3 \times 10^{-5}$ mbar. Reactive sputtering was carried out in a mixture of argon and oxygen. For better oxidation of reactive sputtered Ir atom under the surface of the samples, the oxygen line was extended to the substrate holder. Thus O$_2$ was introduced over the substrate into the sputtering chamber with Ar atmosphere. The sputtering parameters for all the data reported in this paper were O$_2$:Ar $= 1$:2; rate of O$_2$ flow of 2.5 sccm; sputtering pressure of 6.5×10^{-2} mbar, power of the rf generator at 65 W, and 90 min deposition time. The substrate temperature T_s was maintained at 300 °C throughout the entire sputtering process.

2.2. Characterization of iridium dioxide nanocrystals

The IrO$_2$ NCs morphology was studied with a JEOL-JSM6500F FESEM. The dimensions and growth rates of various IrO$_2$ samples were estimated according to the recorded 90° cross-sectional FESEM images. X-ray diffraction data were obtained using a Rigaku D/Max-RC x-ray diffractometer to analyse the crystallographic characteristics of the final NCs over a large area of the surface. The chemical binding state of the IrO$_2$ samples was investigated from Ir 4f and O 1s spectra obtained by x-ray photoelectron spectroscopy (XPS) using the Al Kα1486.68 eV as a radiation source in a Thermo VG Scientific Theta Probe system under the base pressure of 10^{-9} mbar. The Ag 3d$_{5/2}$ line at 368.26 eV was the calibration reference. XPS peak positions and integrated intensities were obtained through curve fitting, using Thermo VG Scientific: Avantage v2.13 Software[5].

Raman scattering spectroscopy was used to extract microstructural information of the IrO$_2$ NCs. Raman measurements were performed using a Renishaw inVia Raman microscope system with an 1800 grooves mm^{-1} grating at room temperature. The 514.5 nm excitation

[5] Thermo V G, Scientific: Avantage Software, West Sussex, UK.
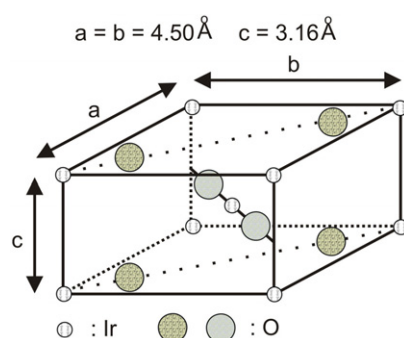
a = b = 4.50Å c = 3.16Å

Figure 2. The unit cell of IrO$_2$ rutile structure.

wavelength beam of an Ar-ion laser (5 mW) was focused to a spot size of $\sim$2 μm in diameter onto the sample using an optical microscope with a 50$\times$ objective. The same microscope was used to collect the signal in backscattering geometry. The scattered light was detected by a charge coupled device (CCD) detection system.

3. Results and discussion

Generally speaking, the substrate structure can play a significant role in controlling the heteroepitaxial deposition of structures as well as in influencing their orientation. In considering the nature of the epitaxial relationships achieved in this work, the surface structures of sapphire substrates and IrO$_2$ NCs have to be examined. IrO$_2$ has the tetragonal rutile structure [41] belonging to the space group D$_{4h}^{14}$ with two IrO$_2$ molecules per unit cell as shown in figure 2. The cations are located at sites with D$_{2h}$ symmetry and the anions occupy sites with C$_{2v}$ symmetry. The Ir ions are surrounded by six oxygen ions at the corners of a slightly distorted octahedron, while the three Ir ions coordinating each oxygen ion lie in a plane at the corners of a nearly equilateral triangle.

3.1. Structure of iridium dioxide nanocrystals on oriented sapphire substrates

3.1.1. Iridium dioxide on SA(001). Scanning electron micrographs shown in figures 3(a) and (b) display images of IrO$_2$ NCs deposited on SA(001) substrate which contains a threefold symmetry surface. FESEM perspective view (figure 3(a)) and cross sectional (figure 3(b)) pictures of NCs on SA(001) exhibited a nanowall-like mosaic structure containing three equivalent structural domains. The estimated dimensions of the nanowalls (NWs) are height $\sim$ 200 nm, thickness and length of the NWs respectively $\sim$20–45 nm and $\sim$100–200 nm. XRD patterns of the IrO$_2$ NWs grown on SA(001) substrate are shown in figure 3(c). The IrO$_2$ (200) diffraction peak at $2\theta = 40.03° \pm 0.02°$ and its higher order reflection of (400) at larger angles $2\theta = 86.40° \pm 0.02°$ exhibit a preferential crystalline alignment of IrO$_2$ NWs along [100] for the sample grown on SA(001).

Heteroepitaxy of IrO$_2$(100) (figure 4(a)) on SA(001) (figure 4(b)) becomes understandable by examining the atomic arrangement of the relevant epitaxy surfaces. The SA(001) surface contains oxygen atoms that exhibit threefold symmetry, and represent the template onto which the NWs are deposited. The lattice parameters for IrO$_2$ are $a = b = 4.4983$ Å and $c = 3.1544$ Å [42], and the lattice parameters for sapphire are $a = b = 4.76$ Å and $c = 12.99$ Å [43]. To compensate for the residual negative charge, the first layer of the IrO$_2$
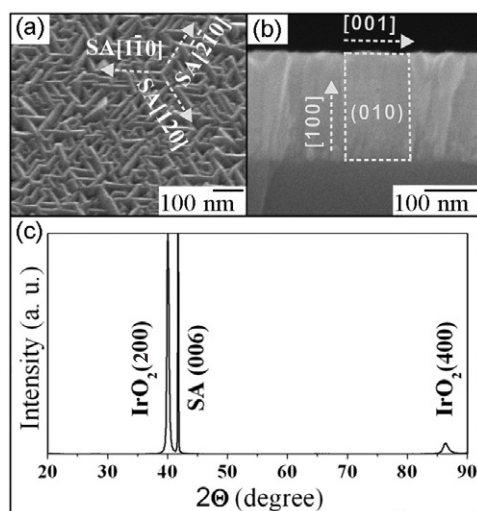
Figure 3. The typical FESEM images: (a) 30° perspective view, (b) cross section view and (c) x-ray diffraction patterns of the in-plane aligned IrO$_2$(100) NCs grown on SA(001).
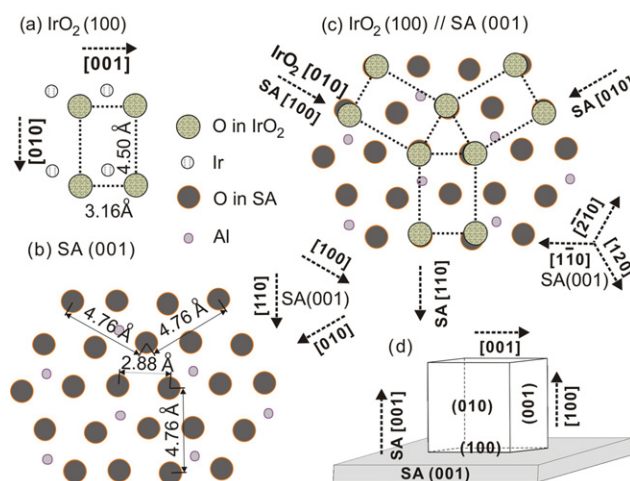

Figure 4. The schematic plots of the lattice relationships between IrO$_2$ NCs and SA(001) substrate: (a) IrO$_2$(100); (b) SA(001); (c) IrO$_2$(100) on SA(001); (d) the schematic drawing of the orientation relationship between IrO$_2$(100) and SA(001).

should be composed of iridium ions. In the IrO$_2$ lattice, each Ir^{4+} is octahedrally coordinated, but termination of the IrO$_2$ lattice with a layer of cations would leave them with a coordination number of three. By centring the metal over a threefold hollow on the oxide surface of SA, each iridium ion can achieve a favourable coordination number of six. The distances between the corner positions in IrO$_2$ are 3.16 and 4.50 Å corresponding, respectively, to the [001] and [010] directions. On SA(001) layers, the distance between the nearest threefold hollow sites is 2.88 Å. Another threefold hollow site in the SA(001) lattice appears every 4.76 Å along the [010], [100] and [110] directions. Thus, if IrO$_2$ NCs are set to grow over SA(100), then the best structural match is to position the IrO$_2$(100) NWs structure such that IrO$_2$[010] ∥ SA[100],
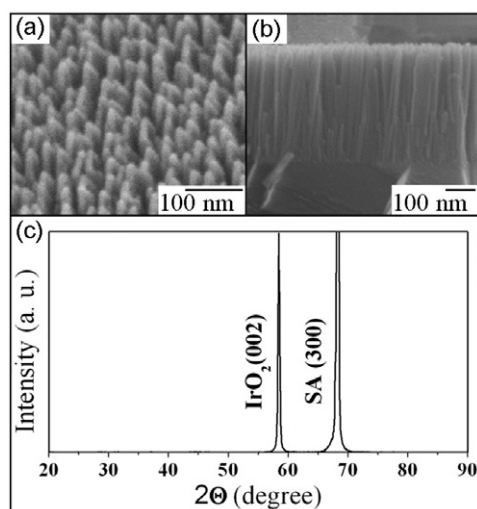
Figure 5. Typical FESEM images: (a) 30° perspective view, (b) cross section view and (c) x-ray diffraction patterns of the vertically aligned $IrO_2(001)$ NCs grown on SA(100).

resulting in a directional mismatch of $+9.72\%$ along $IrO_2[001]$ {i.e. $(3.16–2.88$ Å$)/2.88$ Å}, and -5.46% along $IrO_2[010]$ {i.e. $(4.50–4.76$ Å$)/4.76$ Å}. Schematically, this is marked by the IrO_2 unit cell in figure 4(c), which illustrates the growth of $IrO_2(100)$ NWs on SA(001). In other words, the mismatch is not as energetically favourable along $IrO_2[001]$. Our experimental observation that the IrO_2 NWs take on a mosaic structure consisting of three equivalent domains would be consistent with an epitaxy structure in which IrO_2 unit cells are distributed on the SA(001) surface such that the match along $IrO_2[010]$ is maximized, while that along $IrO_2[001]$ is minimized. Schematically, this is illustrated by the three equivalent unit cells of IrO_2, rotated through 120° from each other, as depicted in figure 4(c). The maximized match of IrO_2 along [010], while that along [001] is minimized, can explain the reason for producing discontinuous growth and forming the nanowall-like structure instead of an epitaxial film.

3.1.2. Iridium dioxide on SA(100). The FESEM images illustrated in figures 5(a) and (b) show fascinating views of the high density vertically aligned IrO_2 NCs grown on a lower symmetry surface—twofold SA(100) substrate. The estimated edge size and the length of the NCs are 40 ± 5 nm and $\sim$400 nm, respectively. The 30° perspective view (figure 5(a)) and cross sectional images (figure 5(b)) of the overall NCs reveal a rod-shaped geometry, and almost all of them have sharp tips. This result indicates that the NCs standing on the substrate are perfectly vertical and have to follow the same in-plane orientation.

The typical XRD patterns of the vertically aligned IrO_2 nanorods (NRs) grown on SA(100) substrate are shown in figure 5(c). A high resolution 2θ scan showed only one diffraction peak at $2\theta = 58.44° \pm 0.02°$, indexable to the $IrO_2(002)$ diffraction signal. No other reflection appeared in the deposition on SA(100) and this confirms the uniquely single-directional growth of IrO_2 NRs along [001] for the sample grown on SA(100). A schematic plot of the IrO_2 NRs on SA(100) is illustrated in figure 6.

An understanding of the heteroepitaxy of IrO_2 on SA at the atomic level can be obtained by examining their (001) (figure 6(a)) and (100) (figure 6(b)) planar structure, respectively. We assume that the surface SA(100) terminated by oxygen atoms are located at the same positions as those found in the single crystal and present a template for the deposition that
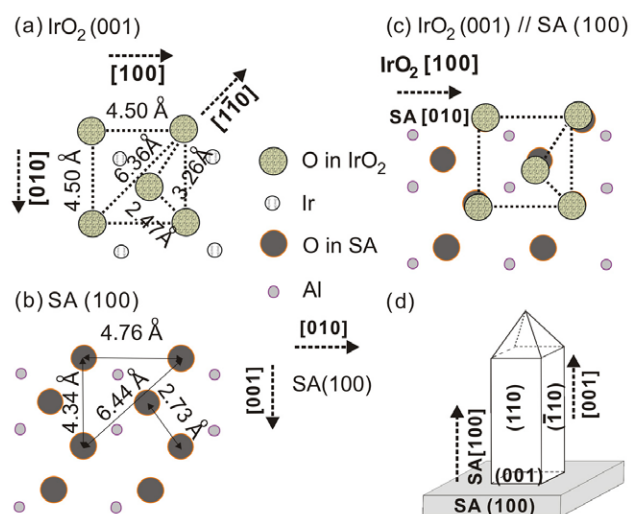
Figure 6. Schematic plots of the lattice relationships between vertical aligned IrO$_2$ NCs and SA(100) substrate: (a) IrO$_2$(001); (b) SA(100); (c) IrO$_2$(001) on SA(100); (d) the schematic drawing of the orientation relationship between IrO$_2$(001) and SA(100).

exhibits twofold symmetry. During the initial stage of NC formation on the substrate surface, the oxygen atoms from the IrO$_2$, formed by reaction of the incoming sputtered Ir atoms from the target and oxygen above the substrate, have sufficient surface mobility to align themselves with the existing oxygen sublattice of the SA(100) in order to form an initial structural network of oxygen atoms. Thus the crystallinity formation follows the in-plane substrate orientation. The distance between corner positions is 4.50 Å in IrO$_2$ for the [100] and [010] directions. The distance between nearest twofold hollow sites in SA(100) is 4.34 Å. Another hollow site in this plane of SA appears every 4.76 Å in the [010] direction. Since the best match planar structure is IrO$_2$(001) on SA(100), a good structural match will align IrO$_2$[100] along SA[010] (figure 6(c)). This nanorod-to-substrate alignment produces an axial residual stress due to mismatch values of -5.46% {i.e. (4.50–4.76 Å)/4.76 Å} along IrO$_2$[100], $+3.69\%$ {(4.50–4.34 Å)/4.34 Å} along IrO$_2$[010] and -1.24% {(6.36–6.40 Å)/6.40 Å} along IrO$_2$[1$\bar{1}$0]. Thus, the mechanism of lattice mismatch based on axial screw growth [1] can be employed to explain the growth of vertically aligned IrO$_2$(001) NRs on SA(100). In this mechanism, an axial stress determines the driving force for the c-axis directional growth.

3.1.3. Iridium dioxide on SA(012) and SA(110). Figures 7(a) and (b) show the FESEM images of high density and well aligned IrO$_2$ NCs grown on a twofold SA(012) substrate, which represent growth on another low symmetry sapphire plane. The self-assembled regularly tilted wedge shaped rod-like NCs were grown with identical tilt angle (~35°) from the normal to the substrate. The estimated dimensions of diameter and length are 40 ± 5 nm and ~400 nm, respectively.

XRD patterns of the IrO$_2$ samples on SA(012) depicted in figure 7(c) showed two peaks at around 34.67° ± 0.02° and 73.2° ± 0.02°, indexed, respectively, as the (101) and (202) planes of the rutile IrO$_2$. These results indicate that all the IrO$_2$(101) planes are parallel to the substrate plane. Figure 8 illustrates the schematic diagram of the orientation relationship between IrO$_2$(101) NRs and the SA(012) substrate. The probable allowed orientation of the
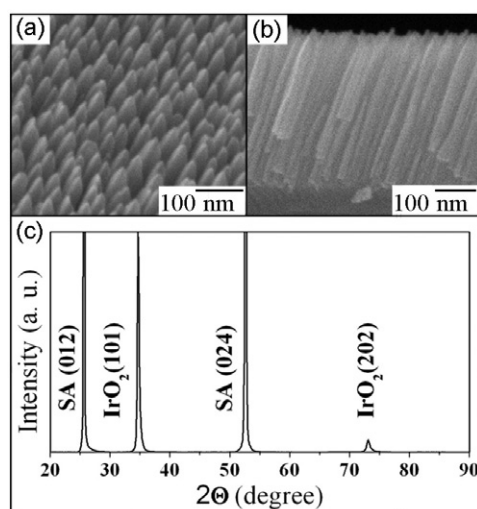
Figure 7. The typical FESEM images: (a) 30° perspective view, (b) cross section view and (c) x-ray diffraction patterns of the single-direction tilted IrO_2 (101) NCs grown on SA(012).
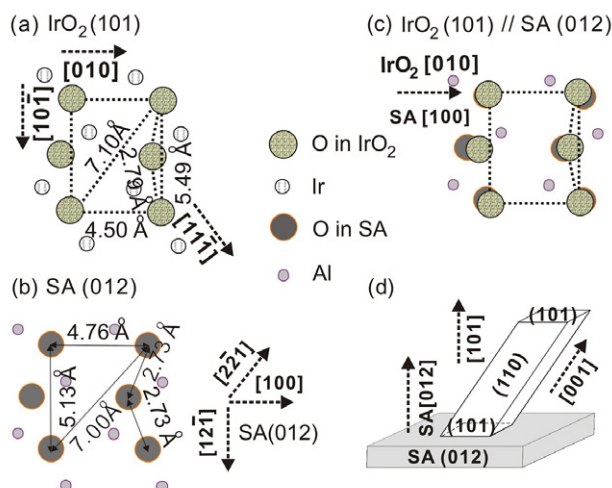

Figure 8. Schematic plots of the lattice relationships between single-direction tilted IrO_2 NCs and SA(012) substrate: (a) $IrO_2(101)$; (b) SA(012); (c) $IrO_2(101)$ on SA(012); (d) schematic drawing of the orientation relationship between $IrO_2(101)$ and SA(012).

NCs deposited on SA(012) substrate or nanorod-to-substrate interface is $IrO_2(101)[010] \parallel$ SA(012)[100].

The obtained heteroepitaxy could be interpreted by examining the planar atomic arrangement of the $IrO_2(101)$ and SA(012) planes (figure 8). The crystallinity formation follows the substrate orientation at conditions when the surface mobility of the sputtered atoms is just sufficient to maintain and sustain the formation of the plane with lowest energy. The orientation that minimizes the lattice misfit and produces the smallest strain energy will be preferred. In accordance with the argument of the minimization of the oxide sublattice structural mismatch mechanism, the best match of $IrO_2(101)$ and SA(012) planes should
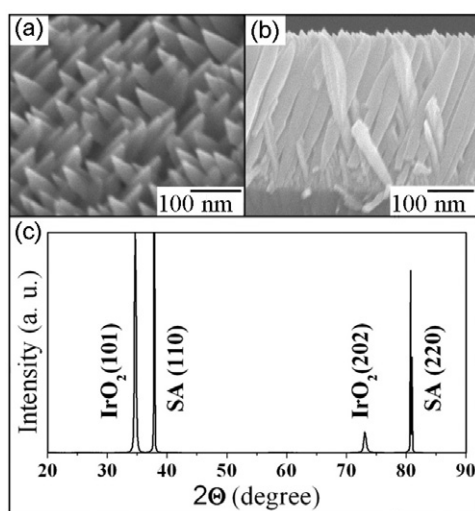
Figure 9. Typical FESEM images: (a) 30° perspective view, (b) cross section view and (c) x-ray diffraction patterns of the symmetrically double-aligned-direction tilted IrO$_2$(101) NCs grown on SA(110).

appear along IrO$_2$[010] ∥ SA[100]. This heteroepitaxy produces directional mismatches of −5.46% {(4.50–4.76 Å)/4.76 Å}, +7.02% {(5.49–5.13 Å)/5.13 Å} and +1.43% {i.e. (7.10–7.00 Å)/7.00 Å} along IrO$_2$[010], IrO$_2$[10$\bar{1}$] and IrO$_2$[11$\bar{1}$], respectively. The formation of tilted NCs schematically depicted in figure 8(d) is the consequence of the two overall mechanisms, in which one is based on the lattice mismatch, termed the axial screw growth mechanism, and the other the c-axis directional growth mechanism [44].

IrO$_2$ NCs deposited on SA(110) substrate exhibit a similar tilt-aligned behaviour as that on the SA(012) substrates. However, the well aligned NCs on SA(110) revealed unique symmetrically double aligned directions rather than the singly tilted one. Figures 9(a) and (b) illustrate, respectively, a 30° perspective and cross sectional views of the symmetrically doubly tilt-aligned directional growth of IrO$_2$ NCs on SA(110). These FESEM images reveal that IrO$_2$ NCs have wedge-like rod structure with average diameter about 40 ± 5 nm and length ∼ 400 nm.

The corresponding XRD patterns for IrO$_2$ deposited on SA(110) shown in figure 9(c) subsequently found that the doubly aligned NRs reveal unique (101) planar deposition on SA(110). These results provide the important information that the doubly aligned IrO$_2$ nanocrystals have a tilt angle of 35° from the normal to the substrate plane, which is the same as IrO$_2$ with a singly tilted alignment on the SA(012) substrates. A schematic diagram of the doubly aligned directional growth of IrO$_2$ on SA(110) is depicted in figure 10. The XRD signals at $2\theta = 34.64° \pm 0.02°$ and $73.08° \pm 0.02°$ assigned to (101) and (202) diffraction planes of rutile IrO$_2$ indicate that a preferential crystalline alignment exhibits the relationship of IrO$_2$(101) ∥ SA(012).

The double directionally tilted alignments become understandable by examining interfaces of the heteroepitaxial growth. The threefold SA(110) surface depicted in figure 10 represents the template structure for the deposition of the twofold symmetrical IrO$_2$(101). The distances between the corner positions in IrO$_2$ are 4.50, 5.49 and 7.10 Å, corresponding to [010], [$\bar{1}$01] and [$\bar{1}\bar{1}$1] directions, respectively. The SA(110) surface exhibits twofold symmetry for the IrO$_2$(101) unit cell. The distance between the nearest twofold hollow sites in the planar
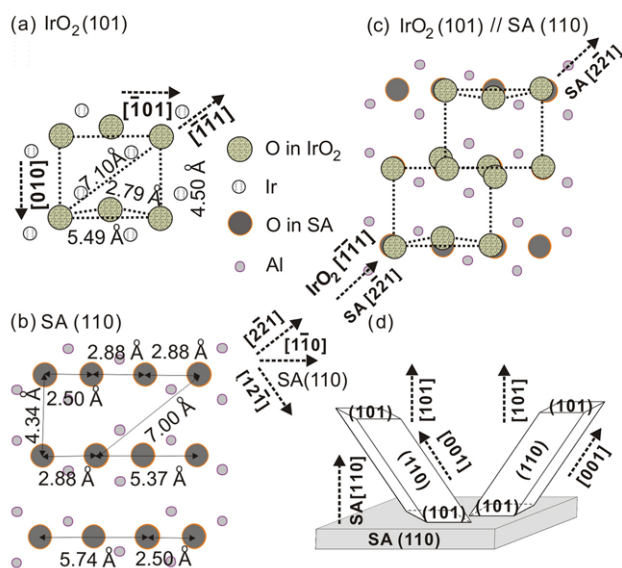
Figure 10. Schematic plots of the lattice relationships between double-aligned-direction tilted IrO_2 NCs and SA(110) substrate: (a) IrO_2(101); (b) SA(110); (c) IrO_2(101) on SA(110); (d) a schematic drawing of the orientation relationship between IrO_2(101) and SA(110).

SA(110) is 4.34 Å. Another twofold hollow site in the SA(110) lattice appears every 8.24 Å along the $[1\bar{1}0]$ direction. The heteroepitaxy of the defined nanocrystal-to-substrate planar alignment should be IrO_2(101) ∥ SA(001). This relationship reveals the possibility to form a mosaic IrO_2(101) structure containing two equivalent structural domains. Thus, the overall orientation relationship between the IrO_2 NRs and SA substrates can be described as the first structural domain, IrO_2(101)$[\bar{1}01]$ ∥ SA(110)$[1\bar{1}0]$ with $IrO_2[\bar{1}\bar{1}1]$ ∥ SA$[2\bar{2}1]$, and the second domain, IrO_2(101) $[\bar{1}01]$ ∥ SA(110) $[\bar{1}10]$ with $IrO_2[11\bar{1}]$ ∥ SA$[2\bar{2}1]$ (figure 10(c)). These two domains have 180° rotation symmetry. The results in the IrO_2(101) NR directional mismatch along [010] will be +3.69 % {(4.50–4.34 Å)/4.34 Å}; −4.36% {(5.49–5.74 Å)/5.74 Å} one side and +2.23% {(5.49–5.37 Å)/5.37 Å} the other side of the unit cell along $IrO_2[\bar{1}01]$, and +1.43% {(7.10–7.00 Å)/7.00 Å} along $IrO_2[\bar{1}\bar{1}1]$. Thus, we can apply the argument of minimization of the oxide sublattice structural mismatch, which is consistent with the axial screw mechanism of directional growth of IrO_2 along the *c*-axis, that is always observed regardless of whether vertical or tilted alignments of the well aligned nanorods were formed.

3.2. XPS investigation

XPS is an appropriate technique to examine the oxidation state and stoichiometry of the oxides. A slow scan XPS was performed on Ir 4f doublet (7/2 and 5/2) and oxygen O 1s peaks in the binding energy ranges of 58–72 eV and 526–540 eV, respectively. Figure 11 shows the peak fitted slow scan XPS spectra of (a) Ir 4f and (b) O 1s core-electron peaks obtained from the reactive sputtered IrO_2(100) NWs deposited on SA(001) substrate. The Gaussian and Lorentzian mixing line shape after treatment of the background by the Shirley function has been used in the fitting to determine the accurate peak positions.

The Ir 4f signal of NWs shows two different binding states of iridium atoms (figure 11(a)). The peaks identified as Ir^{4+} $4f_{7/2}$ and $4f_{5/2}$ at 62.0 and 65.0 eV, respectively, are attributed
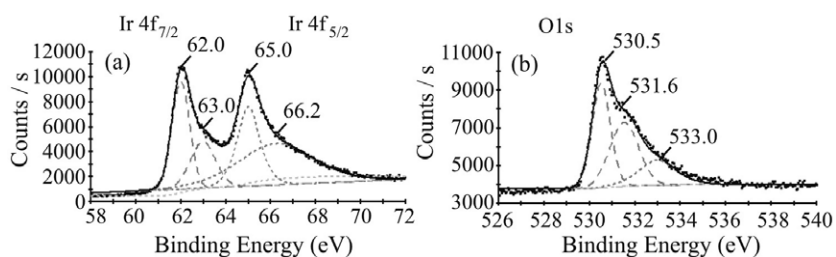
Figure 11. Peak fitted slow scan XPS spectra of (a) the Ir 4f {33.4 at.%} and (b) O 1s {66.6 at.%} lines of the IrO$_2$(100) NCs grown on the SA(001) substrate.
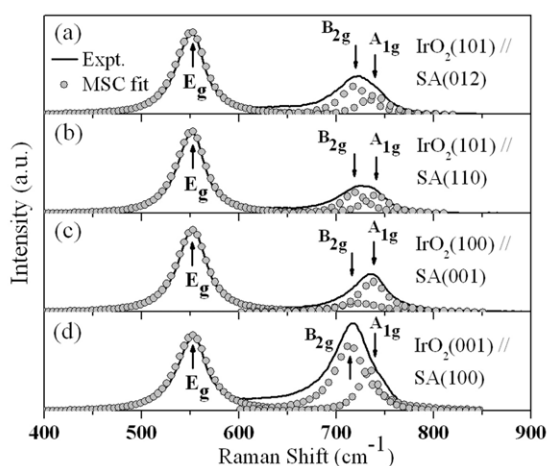

Figure 12. The Raman spectra of the IrO$_2$ NCs deposited on SA substrates (solid lines) and the theoretical results of analysis of the line shape of the E$_g$ mode using an MSC model (open circle lines): (a) IrO$_2$(101) on SA(012); (b) IrO$_2$(101) on SA(110); (c) IrO$_2$(100) on SA(001); (d) IrO$_2$(001) on SA(100).

to the 4+ oxidation state of iridium, and are similar to those of the IrO$_2$ single crystal which have values of 61.7 and 64.7 eV, respectively. Quantitative deconvolution of the XPS spectra revealed two additional features with broader character at 63.0 and 66.2 eV respectively, for the Ir 4f$_{7/2}$ and 4f$_{5/2}$ regions. The XPS results of the O 1s peak (figure 11(b)) show a triplet signal, instead of a single peak in O 1s of the single crystal. The major peak position at about 530.5 eV is the same as that of O 1s of the standard IrO$_2$ single crystal [45] and corresponding to oxygen in the metal–O–metal bond [46]. The oxygen peaks at higher binding energy are situated around 531.6 and 533.0 eV. These extra features located at higher-binding-energy sites of Ir 4f and O 1s indicate the existence of an impurity of higher oxidation states in the IrO$_2$ NWs. Similar spectral features were also observed for IrO$_2$ nanotubes grown by MOCVD [10], RuO$_2$ [47, 48] and OsO$_2$ [49], and attributed to the presence of higher oxidation states. These line shapes of the electron core level are generally observed for the metallic oxides with rutile structure. Quantitative analysis of the peak areas indicates the compositions of the NWs are 33.4 and 66.6 at.% for Ir and O, respectively. The determined Ir/O atomic ratio is about 1/2 and corresponds well to the expected stoichiometry of the IrO$_2$ (100) NWs. Similar XPS spectra were also obtained for IrO$_2$ NCs grown on different orientations of sapphire substrates. The results are summarized in table 1.

Table 1. Binding energies and compositions of the main peaks in the XPS spectra of IrO₂ deposited on SA. The data of the single-crystal IrO₂ [45] are also given for comparison.

Nanocrystals	Binding energies (eV)								Compositions (at.%)	
	Ir $4f_{7/2}$		Ir $4f_{5/2}$		O 1s				Ir	O
IrO₂(100) on SA(001)	62.0	63.0	65.0	66.2	530.5	531.6	533.0		33.4	66.6
IrO₂(001) on SA(100)	62.0	62.9	65.0	66.2	530.5	531.6	533.0		32.4	67.6
IrO₂(101) on SA(012)	62.0	62.9	65.0	66.4	530.5	531.6	533.0		31.6	68.4
IrO₂(101) on SA(110)	62.0	62.9	65.0	66.4	530.5	531.5	533.1		33.6	66.4
IrO₂ single crystal	61.7	—	64.7	—	530.5	—	—		33.3	66.7

3.3. Raman scattering investigation

The first-order Raman spectra of the IrO₂ NCs deposited on SA(012), SA(110), SA(001) and SA(100) are displayed in figures 12(a)–(d), respectively. According to the factor group analysis, the 15 optical modes have the irreducible representations as given in [50]. Only three modes are Raman active in the range of measurements (400–900 cm^{-1}) with symmetries E_g, B_{2g} and A_{1g}, where the first is a doublet and the last two are singlets [51]. Corresponding to each Raman-active mode, there is a scattering tensor α having a distinctive symmetry. The forms of these tensors in materials of the D_{4h}^{14} space group and the displacement of atoms associated with Raman-active modes can be found in [51]. To examine a given component α_{ij}, the geometry is arranged such that the incident light is polarized in the i-direction while only the scattered light of j-polarization is observed.

A classification of the three Raman-active modes for (101), (100) and (001) IrO₂ faces may be accomplished as follows. We adopt the following notation for the various axes used in this experiment: $x = (100)$, $y = (010)$, $z = (001)$ and $x' = 1/\sqrt{2}(10\bar{1})$, $y' = (010)$, $z' = 1/\sqrt{2}(101)$. Since it is impossible to identify the direction in the experiment for NCs we assume that the Raman signal is the average signal from all possible geometries. The expressions for the relative Raman intensities correlating to various $|\alpha_{ij}|^2$ for the (101), (100) and (001) faces in the backscattering configuration are listed in table 2. The results show that E_g, B_{2g} and A_{1g} modes are allowed for the polarization configurations as shown in table 2 for scattering from the (101) face. The B_{2g} and E_g modes are forbidden for all configurations from the (100) and (001) faces, respectively.

The positions of the Raman-active modes for IrO₂ NCs were computed and analysed using the spatial correlation (SC) model of Richter *et al* [52] extended by Fauchet and Campbell [53]. The main assumption is that the phonons in nanometric-sized systems can be confined in space by crystallite boundaries or surface disorders. Consequently, this confinement causes an uncertainty in the wavevector of the phonons and results in downshift and broadening of the Raman features. In this model, the intensity of the first-order Raman spectrum, $I(\omega)$, by taking into account the relaxation of the $q = 0$ selection rule due to phonon confinement in a microcrystal, is given by [53]

$$I(\omega) \cong \int \frac{d^3q \, |C(0, q)|^2}{[\omega - \omega(q)]^2 + (\Gamma/2)^2}, \tag{1}$$

where $\omega(q)$ is the phonon dispersion curve, Γ is the natural linewidth, and $C(0, q)$ is the Fourier coefficient of the phonon confinement function. Using the Gaussian confinement function and considering the column-shaped crystal [53], the Fourier coefficient $|C(0, q)|^2$ can be written as

$$|C(0, q_1, q_2)|^2 \cong e^{-q_1^2 L_1^2/16\pi^2} e^{-q_2^2 L_2^2/16\pi^2} \left| 1 - \text{erf}\left(\frac{iq_2 L_2}{\sqrt{32\pi}}\right) \right|^2, \tag{2}$$

Table 2. Relative Raman intensities of the E$_g$, B$_{2g}$ and A$_{1g}$ phonon modes for the various polarization configurations for IrO$_2$.

	Raman mode		
Polarization configuration	E$_g$	B$_{2g}$	A$_{1g}$
(101) face			
$\alpha_{x'x'}$	e^2	0	$1/4\,(a+b)^2$
$\alpha_{x'y'}$	$1/2\,e^2$	$1/2\,d^2$	0
$\alpha_{y'y'}$	0	0	a^2
(100) face			
α_{zz}	0	0	b^2
α_{zy}	e^2	0	0
α_{yy}	0	0	a^2
(001) face			
α_{xx}	0	0	a^2
α_{xy}	0	d^2	0
α_{yy}	0	0	a^2

where L_1 and L_2 are, respectively, the diameter and length of the IrO$_2$ NCs. For the dispersion relation, $\omega(q)$, we took the analytical model relationship based on a one-dimensional linear-chain model [54]:

$$\omega(q)^2 = A + \{A^2 - B[1 - \cos(\pi q)]\}^{1/2}, \tag{3}$$

where $A = 1.574 \times 10^5$ cm^{-2} and $B = 6.237 \times 10^9$ cm^{-4} (for IrO$_2$ single crystal) related to the atomic masses of the constituent atoms and the force constant between the nearest neighbour planes.

The first-order Raman spectra of the single-direction tilted IrO$_2$(101) NRs deposited on SA(012) illustrated in figure 12(a) revealed three Raman modes, identified as E$_g$, B$_{2g}$ and A$_{1g}$ in the vicinity of the single-crystal signals at 561, 728 and 752 cm^{-1}, respectively [51]. These results are consistent with the assignments given in table 2 and the intensity ratio of Raman-active modes agreed reasonably well with the theoretical prediction. The results of Raman scattering describe the qualitative trend that as the size becomes nanometric the Raman peak shifts to lower frequency and the line-shape becomes asymmetric with a low-frequency tail. Since the intensity of the E$_g$ mode is much larger than that of the other two modes we will focus our SC analysis base on this feature.

The fitted peak positions and FWHM of the Raman E$_g$ mode for the IrO$_2$ NCs deposited on different SA substrates are shown in table 3. The data of the single-crystal IrO$_2$ are also given for comparison. The red-shift in peak position $\Delta\omega$ is a red-shift in the E$_g$ mode peak position as compared with that of the single crystal. Our calculated results of the red-shift for IrO$_2$ (101) on the SA(012) sample using the SC model indicated a 6.4 cm^{-1} red-shift and an asymmetric broadening of 31 cm^{-1} relating to the phonon confinement effect in NCs. In order to have a good agreement between SC model calculations and experimental data we have to add an additional red-shift of $\sim$3 cm^{-1} to the SC model. We have tentatively assigned this shift to the residual stress effect. Rosenblum *et al* [55] reported observation of a blue-shift on the three strongest lines induced by hydrostatic pressure in the RuO$_2$ single crystal, which is consistent with our results of the red-shift induced by tensile strain. In order to correlate experimental data with our theoretical modelling we have to include an additional red-shift of 3 cm^{-1} in the SC model and recalculate the constants for the analytical model of dispersion relation as given

Table 3. The fitted peak positions, FWHM, red-shift ($\Delta\omega$) of the E_g mode and average diameter (L_1) of the IrO$_2$ NCs deposited on different SA substrates. $\Delta\omega_{\text{size}}$ and $\Delta\omega_{\text{stress}}$ red-shift related to phonon confined and residual stress effects, respectively. The data of the single-crystal IrO$_2$ [51] are also given for comparison.

Nanocrystals	Raman mode					
	E_g (cm^{-1})	FWHM (cm^{-1})	$\Delta\omega$(cm^{-1})	$\Delta\omega_{\text{size}}$ (cm^{-1})	$\Delta\omega_{\text{stress}}$ (cm^{-1})	L_1 (nm)
IrO$_2$(101) ∥ SA(012)	551.6	31	9.4	6.4	3	39
IrO$_2$(101) ∥ SA(110)	551.9	30	9.1	6.1	3	40
IrO$_2$(100) ∥ SA(001)	552.6	33	8.4	5.4	3	44
IrO$_2$(001) ∥ SA(100)	552.7	36	8.3	5.3	3	45
IrO$_2$ single crystal	561.0	12	—	—	—	—

by equation (3). Our analysis gives $A = 1.557 \times 10^5$ cm^{-2} and $B = 6.105 \times 10^9$ cm^{-4} for the series of IrO$_2$ NCs structures used in these experiments. Using our proposed MSC model, which includes the effect of the residual stress, we are able to correlate the measured red-shift of the Raman active modes as due to nanometric size and residual stress effect. As shown in figure 12(a), the open circle lines indicate the theoretical calculations using the MSC model. The agreement of the experimental data for the E_g phonon mode peak and the calculated result with diameter $L_1 = 39$ nm is reasonably good. It should be noted that the diameters used as the correlation length in the MSC model are the average diameters estimated from the FESEM images.

Figure 12(b) shows the Raman spectra of the IrO$_2$(101) NCs on SA(110) and fitting results (open circle lines) in the range of 400–900 cm^{-1}, in which three Raman modes, identified as E_g, B_{2g} and A_{1g}, were observed. These results show a good agreement with the selection rules indicated in table 2. By analysing the main scattering signal of the E_g mode, the NCs exhibit a ∼9.1 cm^{-1} red-shift in peak position and asymmetric broadening ∼ 30 cm^{-1}. The analysis in the MSC model revealed 6.1 cm^{-1} in red-shift as a result of the phonon confinement effect and an additional 3 cm^{-1} shift due to residual stress effect. We also believe that observation of E_g, B_{2g} and A_{1g} modes in the Raman experiment with the intensity of the E_g peak much larger than the overlapped signal of B_{2g} and A_{1g} modes can be evidence of orientation of NCs in the (101) plane. From the experimental data, the singly tilted NRs revealed higher intensity of the B_{2g} peak in comparison with the A_{1g} mode, whereas for the doubly tilted NRs the intensities of B_{2g} and A_{1g} modes as analysed by the MSC model are comparable.

In figure 12(c) we show the Raman results of the IrO$_2$ (100) NCs deposited on SA(001). Comparison of this figure with table 2 allows us to identify the allowed E_g and A_{1g} Raman modes. The weak intensity of the normally forbidden B_{2g} mode as extracted by the MSC indicates good agreement with the theoretical prediction as given in table 2. The additional red-shift of ∼3 cm^{-1} induced by a residual stress has been included in the MSC model ($L_1 = 44$ nm) for the adequate description of the 8.4 cm^{-1} downshift of the E_g mode peak (552.6 cm^{-1}, FWHM = 33 cm^{-1}) (table 3). Thus, the Raman result of IrO$_2$ NWs deposited on SA(001) is consistent with the XRD result of these samples and confirms the presence of the IrO$_2$ (100) plane.

The Raman spectrum of the vertically aligned IrO$_2$(001) NCs deposited on SA(100) and the E_g mode fitting results are illustrated in figure 12(d). The micro-Raman spectrum revealed three Raman mode signals that are inconsistent with the allowed modes for the (001) face (table 2). We observe the signal of the forbidden E_g mode for this configuration with intensity slightly less than that of the overlapped signal of B_{2g} and A_{1g} modes. The occurrence of the normally forbidden E_g mode might indicate observation of the scattering from other planes of the NCs as evidenced from the pyramidal tips of the NRs (figure 7(d)) and/or from the strain

induced Raman tensor which may break down the selection rules. The soft E$_g$ signal can be evidence of the rod-like vertically aligned IrO$_2$ NCs with (001) orientation.

The observed red-shift and asymmetric line width broadening of the Raman signal are attributed to both the size and residual stress effects, and can be satisfactorily explained by the MSC model. In general, the intensities of the Raman signal followed the selection rules for different planes of IrO$_2$ NCs. Observation of the normally forbidden Raman modes can be explained by the existence of stress and/or rod-shape NCs with pyramidal tips along the *c*-axis.

4. Conclusion

Well aligned densely packed IrO$_2$ nanocrystals have been grown on SA(001), SA(100), SA(012) and SA(110) substrates via rf magnetron sputtering. The results of the structural study reveal that the IrO$_2$(100) NWs grown on SA(001) have a mosaic structure with three equivalent structural domains rotated through 120° from each other. Vertically aligned IrO$_2$ (001) NRs are also grown on SA(100), while the NRs deposited on the SA(012) and SA(110) are grown with a tilt angle of $\sim$35° (IrO$_2$(101)) from the normal to the substrates. Moreover, the NRs on SA(110) reveal symmetrical doubly aligned tilted NRs, instead of the singly aligned tilted NRs on SA(012). The strong substrate effect on the alignment of the IrO$_2$ NCs during growth has been demonstrated. The vertical or singly or doubly tilted alignment of the IrO$_2$ NCs can be understood by the mechanism of lattice mismatch at the interfaces of IrO$_2$ and SA substrates. Directional growth of IrO$_2$ along the *c*-axis is always observed, regardless of whether nanowalls or rods are formed. XPS analysis indicate the existence of an impurity of higher oxidation states in the IrO$_2$ NCs.

The micro-Raman scattering results reveal three Raman-active modes, identified as E$_g$, B$_{2g}$ and A$_{1g}$, around 552, 719 and 743 cm^{-1}, respectively. The Raman scattering intensity of certain modes depends on planes of NCs and follows the selection rules reasonably well. The analysis indicates a possibility to determine the preferable growth direction of NCs using Raman scattering. The red-shifts and asymmetric line shape with a low-frequency tail can be satisfactorily described by a modified spatial correlation model which includes phonon confinement and stress induced effects. The MSC model analysis of the observed Raman features can also be utilized as a useful technique for the estimation of the residual stress in the nanostructures.

Acknowledgments

References

[1] Xia Y, Yang P, Sun Y, Wu Y, Mayers B, Gates B, Yin Y, Kim F and Yan H 2003 *Adv. Mater.* **15** 353
[2] Patzke G R, Krumeich F and Nesper R 2002 *Angew. Chem. Int. Edn Engl.* **41** 2446
[3] Hu J, Odom T W and Lieber C M 1999 *Acc. Chem. Res.* **32** 435
[4] Zhu Y Q, Hu W B, Hsu W K, Terrones M, Grobert N, Hare J P, Kroto H W, Walton D R M and Terrones H 1999 *J. Mater. Chem.* **9** 3173
[5] Pradhan S K, Reucroft P J, Yang F and Dozier A 2003 *J. Cryst. Growth* **256** 83
[6] Liu Y, Dong J and Liu M 2004 *Adv. Mater.* **16** 353
[7] Bai Z G, Yu D P, Zhang H Z, Ding Y, Wang Y P, Gai X Z, Hang Q L, Xiong G C and Feng S Q 1999 *Chem. Phys. Lett.* **303** 311
[8] Choi Y C, Kim W S, Park Y S, Lee S M, Bae D J, Lee Y H, Park G S, Choi W B, Lee N S and Kim J M 2000 *Adv. Mater.* **12** 746

[9] Muhr H J, Krumeich F, Schonholzer U P, Bieri F, Niederberger M, Gauckler L J and Nesper R 2000 *Adv. Mater.* **12** 231

[10] Chen R S, Chang H M, Huang Y S, Tsai D S, Chattopadhyay S and Chen K H 2004 *J. Cryst. Growth* **271** 105

[11] Mattheiss L F 1976 *Phys. Rev.* B **13** 2433

[12] Pinnow C U, Kasko I, Nagel N, Poppa S, Mikolajick T, Dehm C, Hosler W, Bleyl F, Jahnel F, Seibt M, Geyer U and Samwer K 2002 *J. Appl. Phys.* **91** 9591

[13] Horng R H, Wuu D S, Wu L H and Lee M K 2000 *Thin Solid Films* **373** 231

[14] Liao P C, Ho W S, Huang Y S and Tiong K K 1998 *J. Mater. Res.* **13** 1318

[15] Ges I A, Ivanov B L, Schaffer D K, Lima E A, Werdich A A and Baudenbacher F J 2005 *Biosens. Bioelectron.* **21** 248

     Wang M, Yao S and Madou M 2002 *Sensors Actuators* B **81** 313

[16] Pasztor K, Sekiguchi A, Shimo N, Kitamura N and Masuhara H 1993 *Sensors Actuators* B **12** 225

[17] Yao S, Wang M and Madou M 2001 *J. Electrochem. Soc.* **148** H29

[18] Smiechowski M F and Lvovich V F 2003 *Sensors Actuators* B **96** 261

[19] Kotz E R and Neff H 1985 *Surf. Sci.* **160** 517

[20] Osaka A, Takatsuna T and Miura Y 1994 *J. Non-Cryst. Solids* **178** 313

[21] Ioroi T, Kitazawa N, Yasuda K, Yamamoto Y and Takenaka H 2000 *J. Electrochem. Soc.* **147** 2018

[22] Sakoda T, Moise T S, Summerfelt S R, Colombo L, Xing G, Gilbert S R, Loke A L S, Ma S, Kavari R, Wills L A and Amano J 2001 *Japan. J. Appl. Phys.* 1 **40** 2911

[23] Jo W 2001 *Appl. Phys.* A **72** 81

[24] Cogan S F, Plante T D, McFadden R S and Rauh R D 1987 *Sol. Energy Mater.* **16** 371

[25] Yamanaka K 1989 *Japan. J. Appl. Phys.* **28** 632

[26] Chalamala B R, Wei Y, Rossi G, Smith B G and Reuss R H 2000 *Appl. Phys. Lett.* **77** 3284

[27] Kuratani Y, Morikawa Y and Okuyama M 1998 *Japan. J. Appl. Phys.* **37** 5421

[28] Chiang D, Lei P Z, Zhang F and Barrowcliff R 2005 *Nanotechnology* **16** S35

[29] Chen R S, Huang Y S, Liang Y M, Hsieh C S, Tsai D S and Tiong K K 2004 *Appl. Phys. Lett.* **84** 1552

[30] Pinnow C U, Kasko I, Dehm C, Jobst B, Seibt M and Geyer U 2001 *J. Vac. Sci. Technol.* B **19** 1857

[31] El Khakani M A and Chaker M 1998 *Thin Solid Films* **335** 6

[32] Serventi A M, El Khakani M A, Saint-Jacques R G and Rickerby D G 2001 *J. Mater. Res.* **16** 2336

[33] Pickup P G and Birss V I 1988 *J. Electrochem. Soc.* **135** 126

[34] Belova I D, Varlamova T V, Galyamov B Sh, Roginskaya Yu E, Shifrina R R, Prutchenko S G, Kaplan G I and Sevostyanov M A 1988 *Mater. Chem. Phys.* **20** 39

[35] Music S, Popovic S, Maljkovic M, Skoko Z, Furic K and Gajovic A 2003 *Mater. Lett.* **57** 4509

[36] Chen R S, Chen Y S, Huang Y S, Chen Y L, Chi Y, Liu C S, Tiong K K and Carly A J 2003 *Chem. Vapor Depos.* **9** 301

[37] Chen R S, Huang Y S, Liang Y M, Tsai D S, Chi Y and Kai J J 2003 *J. Mater. Chem.* **13** 2525

[38] Chen R S, Chang H M, Huang Y S, Tsai D S, Chattopadhyay S and Chen K H 2004 *J. Cryst. Growth* **271** 105

[39] Chen R S, Huang Y S, Tsai D S, Chattopadhyay S, Wu C T, Lan Z H and Chen K H 2004 *Chem. Mater.* **16** 2457

[40] Chen R S, Chang H M, Huang Y S, Tsai D S and Chiu K C 2005 *Nanotechnology* **16** 93

[41] Xu J H, Jarlborg T and Freeman A J 1989 *Phys. Rev.* B **40** 7939

[42] JCPDS card no. 15-870 (IrO$_2$), International Centre for Diffraction Data, Newtown Square, PA, USA

[43] JCPDS Card No.10-0173 (Al$_2$O$_3$), International Centre for Diffraction Data, Newtown Square, PA, USA

[44] Chen C C, Chen R S, Tsai T Y, Huang Y S, Tsai D S and Tiong K K 2004 *J. Phys.: Condens. Matter* **16** 8475

[45] Liao P C, Chen C S, Ho W S, Huang Y S and Tiong K K 1997 *Thin Solid Films* **301** 7

[46] Hara M, Asami K, Hashimoto K and Masumoto T 1986 *Electrochim. Acta* **31** 481

[47] Bhaskar S, Dobal P S, Majumder S B and Katiyar R S 2001 *J. Appl. Phys.* **89** 2987

[48] Chan H Y H, Takoudis C G and Weaver M J 1997 *J. Catal.* **172** 336

[49] Sarma D D and Rao C N R 1980 *J. Electron Spectrosc. Relat. Phenom.* **20** 25

[50] Loudon 1964 *Adv. Phys.* **13** 423

[51] Huang Y S, Lin S S, Huang C R, Lee M C, Dann T E and Chien F Z 1989 *Solid State Commun.* **70** 517

[52] Richter H, Wang Z P and Ley L 1981 *Solid State Commun.* **39** 625

[53] Campbell I H and Fauchet P M 1986 *Solid State Commun.* **58** 739

[54] Kittel C 1996 *Introduction to Solid State Physics* 7th edn (New York: Wiley) p 106

[55] Rosenblum S S, Weber W H and Chamberland B L 1997 *Phys. Rev.* B **56** 529